Pergamon

*Int. J. Heat Mass Transfer.* Vol. 39, No. 13, pp. 2751–2770, 1996
Copyright © 1996 Elsevier Science Ltd
Printed in Great Britain. All rights reserved
0017-9310/96 $15.00 + 0.00

0017-9310(95)00348-7

# Flow and transport in a multilayered fluid system—I. Influence of 1- or $\mu$-*g* environment

J.-P. FONTAINE† and R. L. SANI

Center for Low-Gravity, Department of Chemical Engineering, University of Colorado, Boulder, CO 80309, U.S.A.

(*Received* 22 *February* 1993 *and in final form* 28 *July* 1995)

**Abstract**—The combined effects of thermocapillary and buoyancy forces in an open cavity heated from one side have been modeled numerically. The configuration is that of two shallow, immiscible superposed liquid layers. High Prandtl number fluids are considered under both 1- and $\mu$-*g* environments. The interfaces are considered deformable. It is shown that encapsulation strongly reduces the flow in the lower layer, and that a $\mu$-g environment significantly reduces the flow in the lower layer. The sensitivity of the flow structure to some physical properties is also described, and particularly the relevance of the thermocapillary forces.
Copyright © 1996 Elsevier Science Ltd.

## 1. INTRODUCTION

The study of the behavior of fluid flow and convective heat transfer in a system composed of different superposed fluid layers (liquid or gas) is of interest in many engineering applications. One important area is crystal growth and in particular, growth in a micro-gravity space environment where it is hoped that high quality, large size crystals can be grown. Reduction of the gravity level leads to a reduction in natural convection and of the hydrostatic pressure level (two suspected sources of imperfections in crystal growth on earth). However, then convective effects associated with surface tension driven flows oftentimes become very important; that is, the presence of a variation in interfacial tension can affect and/or generate fluid flow [1, 2]. One way to minimize the surface tension effect is by the use of an encapsulant layer as in a liquid-encapsulated Czochralski configuration where liquid boron oxide (high viscosity) covers a gallium arsenide melt. In this case the encapsulant layer also prevents evaporation of volatile components like arsenic [3]. In fact the analysis of the behavior of such phenomena is currently of major interest since there are space experiments planned which involve multi-layered systems.

This numerical study concerns the prediction and the analysis of the flow structure and concomitant heat transfer which develop in a differentially heated rectangular cavity containing shallow, immiscible fluid layers. In this study high Prandtl number fluids are considered. A space experiment of such a multilayered system using the Bubble Drop and Particle Unit (BDPU) built by the European Space Agency is planned for the IML-2 mission scheduled for 1994 [4, 5]. One aim of the space experiment is to find criteria to reduce the surface tension driven flow in the lower liquid layer which is presumed to be representative of an encapsulated melt of an electronic material, although presently no low Prandtl number fluids are investigated. This study was initiated to aid in the definition of the space flight experiment as well as post-flight data analysis. This work was performed in collaboration with the ground-based experiments in progress by Koster *et al.* [4, 5], where the gravitational force is oriented perpendicular to the interfaces.

The first phase of this numerical study (see ref. [6]) focused on an open, shallow cavity, heated from one side and filled with a high Prandtl number fluid (taken to be fluorinert FC75) in a terrestrial environment, in order to compare with the experiments [4, 5]. The combined effects of buoyancy and thermocapillary forces have been analyzed for various experimental conditions. A significant influence of the thermocapillary forces on the form of the bulk flow in such systems has been shown [6]. The second phase described herein concerns a two layer system of immiscible liquids where the upper interface is a free surface. Both the top and the intermediate liquid–liquid interface are considered deformable. This configuration is subjected to 1- and $\mu$-*g* conditions. The aim is to show the contribution of a low-gravity environment. First, the evolution of the flow structure when increasing the temperature contrast between the two side walls was studied for a fluorinert FC75–water system under both 1- and $\mu$-*g* environments (see also refs. [7, 8]). The sensitivity of the nature of the flow to some physical properties of the upper liquid is described herein.

† Institut de Mécanique des Fluides, C.N.R.S.-U.M.34 and I.R.P.H.E., C.N.R.S.-U.M.138, 1, rue Honnorat, 13003 Marseille, France. Present address: I.M.R.A. Europe S.A., B.P. 213, 220 r. A. Caquot, 06904 Sophia-Antipolis, France.

## NOMENCLATURE

| | |
|---|---|
| $A = H/L$ | aspect ratio of each layer |
| $Bd$ | dynamic Bond number |
| $Ca$ | Capillary number |
| $\mathbf{e}_x$, $\mathbf{e}_y$ | unit vectors |
| $Fr$ | Froude number |
| $g$ | gravitational acceleration |
| $Gr$ | Grashof number |
| $H$ | height of each liquid layer |
| $\mathscr{H}$ | mean Gaussian curvature |
| $k$ | thermal conductivity |
| $L$ | length of the cavity |
| $Ma$ | Marangoni number |
| $\mathbf{n}$ | unit outward pointing normal vector |
| $p$ | static pressure |
| $Pr$ | Prandtl number |
| $R_\sigma$ | surface tension Reynolds number |
| $\mathbf{t}$ | unit tangent vector. |
| $T$ | temperature |
| $U$ | velocity scale |
| $u$ | horizontal component of the velocity |
| $v$ | vertical component of the velocity |
| $x$ | horizontal axis |
| $y$ | vertical axis. |

Greek symbols

| | |
|---|---|
| $\beta$ | volumetric coefficient of thermal expansion |
| $\gamma$ | temperature coefficient of surface tension |
| $\mu$ | dynamic viscosity |
| $\nu$ | kinematic viscosity |
| $\rho$ | density |
| $\sigma$ | surface tension coefficient |
| $\tau$ | stress tensor |
| $\phi$ | contact angle of a liquid |
| $\chi$ | thermal diffusivity. |
| $\psi$ | streamfunction. |

Subscripts

| | |
|---|---|
| c | cold |
| h | hot |
| 0 | reference state |
| 1 | lower layer ($j = 1$ or 2) |
| 2 | upper layer. |

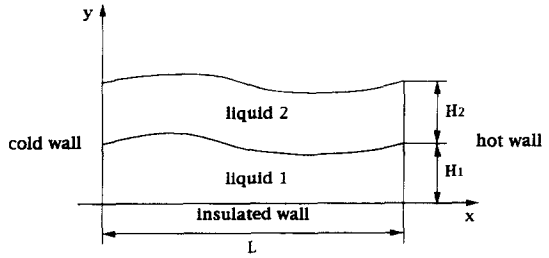


Fig. 1. Schematic diagram of the multilayered system.

## 2. PHYSICAL MODEL

The configuration consists of two immiscible liquid layers of equal volume contained in a two-dimensional open cavity (Fig. 1). An aspect ratio of $A = H/L = 1/5.1$ (where $H$ is the height and $L$ the length) representing Koster's experiments [4, 5] has been considered for each layer. A temperature gradient is imposed perpendicular to the gravitational force by maintaining the isothermal side walls at different temperatures. The upper interface is taken to be a free surface, representative of a liquid–gas interface. Both the top and the intermediate liquid–liquid interface are deformable, but with fixed contact angles and subjected to surface tension gradients induced by the temperature gradient along each interface. At this time the contact angles $\phi$ have been taken equal to $\phi = \pi/2$, like in our one layer model [6]. Further modeling studies including wetting and non-wetting liquids are planned since Keller and Bergman [9] or Kamotani [10] have shown that there can be some significant effects in these cases when taking into account a deformable interface (see ref. [6]).

The fluids considered were the fluorinert FC75 for the lower layer and in most cases water for the upper one, a system which is gravitationally stable, i.e. the density of FC75 is larger than that of water.

## 3. MATHEMATICAL MODEL

In the mathematical model, like for the one liquid layer configuration [6], the flow in each liquid phase is assumed to be laminar, the fluid to be Newtonian and the Boussinesq approximation is made. That is, physical properties such as viscosity, density (except in the buoyancy term), volumetric coefficient of thermal expansion, temperature coefficient of surface tension, heat capacity, thermal diffusivity, conductivity are assumed to be constant.

The fluid density in the body force term in the Boussinesq approximation is modeled using

$$\rho = \rho_0[1-\beta(T-T_0)] \tag{1}$$

where the subscript 0 refers to a reference state

$$\beta = -\frac{1}{\rho_0}\frac{\partial \rho}{\partial T}\bigg|_{T_0}$$

is the volumetric coefficient of thermal expansion, $\rho$ is the density, and $T$ is the temperature.

As proposed by Cuvelier and Driessen [11] the following Boussinesq type approximation with respect to the surface tension is made: the surface tension

coefficient $\sigma$ equals a constant value $\sigma_0$ independent of temperature, except in the tangential force boundary condition, where $\sigma$ is considered to be a linear function of temperature

$$\sigma = \sigma_0[1-\gamma(T-T_0)] \tag{2}$$

where

$$\gamma = -\frac{1}{\sigma_0}\frac{\partial\gamma}{\partial T}\bigg|_{T_0}$$

is the temperature coefficient of surface tension. (For many high Prandtl number liquids the value of $\gamma$ is positive.)

The governing equations are mass conservation and the coupled Navier–Stokes and energy equations. The flow is assumed to be steady in the initial phase of this work. To non-dimensionalize the variables let

$$x_j^i = \frac{x_j^{*i}}{L} \quad u_j^i = \frac{u_j^{*i}}{U} \quad p_j = \frac{p_j^*}{\rho_1 U^2} \quad T_j = \frac{T_j^* - T_0}{T_h - T_c} \tag{3}$$

where * denotes dimensional quantities, $T_h$ and $T_c$ are the hot and cold side wall temperatures, respectively ($\Delta T = T_h - T_c$), $U$ is the velocity scale, $p$ is the static pressure, $i$ denotes the different vector components and $j$ refers to the liquid layer (1 for the lower and 2 for the upper).

As in our one liquid layer model [6], the velocity scale suggested by Ostrach [12, 13] for a boundary layer type of flow in $\mu$-g was used

$$U = \left[\left(\frac{\partial\sigma_1}{\partial T}\right)^2 \frac{(T_h - T_c)^2 \nu_1}{\mu_1^2 L}\right]^{1/3} \tag{4}$$

where $\nu$ is the kinematic viscosity and $\mu$ the dynamic viscosity.

Finally, the dimensionless problem is formulated as follows:

lower layer

$$\nabla\cdot\mathbf{u} = 0 \tag{5}$$

$$(\mathbf{u}\cdot\nabla)\mathbf{u} = -\nabla p - \frac{1}{Fr}\left(1 - \frac{Fr\,Gr_1}{R_{\sigma_1}^{4/3}}T\right)\mathbf{e}_y + \frac{1}{R_{\sigma_1}^{2/3}}\nabla\cdot\boldsymbol{\tau} \tag{6}$$

$$\mathbf{u}\cdot\nabla T = \frac{1}{Pr_1 R_{\sigma_1}^{2/3}}\nabla^2 T \tag{7}$$

upper layer

$$\nabla\cdot\mathbf{u} = 0 \tag{8}$$

$$\hat{\rho}(\mathbf{u}\cdot\nabla)\mathbf{u} = -\nabla p - \hat{\rho}\frac{1}{Fr}\left(1 - \hat{\beta}\frac{Fr\,Gr_1}{R_{\sigma_1}^{4/3}}T\right)\mathbf{e}_y + \hat{\mu}\frac{1}{R_{\sigma_1}^{2/3}}\nabla\cdot\boldsymbol{\tau} \tag{9}$$

$$\hat{\rho}\mathbf{u}\cdot\nabla T = \hat{\mu}\frac{1}{Pr_2 R_{\sigma_1}^{2/3}}\nabla^2 T \tag{10}$$

where $\tau = \mu(\nabla\mathbf{u} + \nabla\mathbf{u}^t)$ is the stress tensor, $\mathbf{u} = u\mathbf{e}_x + v\mathbf{e}_y$ is the velocity vector, $(\mathbf{e}_x, \mathbf{e}_y)$ are unit vectors, $x$ is the horizontal axis, $y$ is the vertical one,

$$\hat{\rho} = \frac{\rho_{02}}{\rho_{01}}, \quad \hat{\beta} = \frac{\beta_2}{\beta_1} \quad \text{and} \quad \hat{\mu} = \frac{\mu_2}{\mu_1}.$$

The dimensionless parameters which appear are the Grashof number

$$Gr_j = \frac{g\beta_j \Delta T L^3}{\nu_j^2},$$

the Prandtl number, $Pr_j = \nu_j/\chi_j$, the Froude number, $Fr = U^2/gL$, and the surface tension Reynolds number

$$R_{\sigma_j} = \left|\frac{\partial\sigma_j}{\partial T}\right|\frac{\Delta T L}{\mu_j \nu_j}.$$

Two other parameters will also be used, the Marangoni number

$$Ma_j = \left|\frac{\partial\sigma_j}{\partial T}\right|\frac{\Delta T L}{\mu_j \chi_j} \quad (Ma = Pr\,R_\sigma),$$

and the dynamic Bond number

$$Bd_j = \frac{\beta_j \rho_{0j} g L^2}{\gamma_j \sigma_{0j}} \quad (Bd_j = Gr_j Pr_j / Ma_j)$$

where $g$ is the gravitational acceleration and $\chi$ the thermal diffusivity.

No-slip and no-penetration conditions are imposed along the rigid walls. The vertical sides are maintained at constant temperatures (hot and cold); the reference temperature has been taken as $T_0 = T_c$. The bottom of the cavity is assumed to be thermally insulated. These boundary conditions are written as follows:

$$x = 0, \quad 0 \leqslant y < A \quad \text{and} \quad A < y < 2A$$
$$u = v = 0 \quad T = 0 \tag{11}$$

$$x = 0, \quad y = A \quad \text{and} \quad y = 2A \quad u = 0 \quad T = 0 \tag{12}$$

$$0 \leqslant x \leqslant 1, \quad y = 0 \quad u = v = 0 \quad \frac{\partial T}{\partial y} = 0 \tag{13}$$

$$x = 1, \quad 0 \leqslant y < H_1(1) \quad \text{and} \quad H_1(1) < y < H_2(1)$$
$$u = v = 0 \quad T = 1 \tag{14}$$

$$x = 1, \quad y = H_1(1) \quad \text{and} \quad y = H_2(1)$$
$$u = 0 \quad T = 1 \tag{15}$$

where $H_j(x)$ is the location of the moving interface $j$.

At the deformable interfaces the following boundary conditions are obtained from mass conservation, kinematic constraints, and normal and tangential stress balances (for $x > 0$):

Liquid–gas interface

$$\mathbf{u}_2\cdot\mathbf{n}_2 = 0 \tag{16}$$

$$-p_2+\hat{\mu}\frac{1}{R_{\sigma_1}^{2/3}}\mathbf{n}_2\mathbf{n}_2:\tau=2\hat{\sigma}\mathscr{H}_2\left(\frac{1}{Ca_{01}R_{\sigma_1}^{2/3}}-\hat{\gamma}\frac{1}{R_{\sigma_1}^{1/3}}T_2\right) \tag{17}$$

$$\hat{\mu}\frac{1}{R_{\sigma_1}^{2/3}}\mathbf{t}_2\mathbf{n}_2:\quad \tau=-\hat{\sigma}\hat{\gamma}\frac{1}{R_{\sigma_1}^{1/3}}\mathbf{t}_2\cdot\nabla T_2 \tag{18}$$

$$\mathbf{n}_2\cdot\nabla T_2=0 \tag{19}$$

Liquid–liquid interface

$$\mathbf{u}_1\cdot\mathbf{n}_1=\mathbf{u}_2\cdot\mathbf{n}_1=0 \tag{20}$$

$$-(p_1-p_2)+\frac{1}{R_{\sigma_1}^{2/3}}(1-\hat{\mu})\mathbf{n}_1\mathbf{n}_1:$$

$$(\tau_1-\tau_2)=2\mathscr{H}_1\left(\frac{1}{Ca_{01}R_{\sigma_1}^{2/3}}-\frac{1}{R_{\sigma}^{1/3}}T\right) \tag{21}$$

$$\frac{1}{R_{\sigma_1}^{2/3}}(1-\hat{\mu})\mathbf{t}_1\mathbf{n}_1:\quad(\tau_1-\tau_2)=-\frac{1}{R_{\sigma_1}^{1/3}}\mathbf{t}_1\cdot(\nabla T_1+\nabla T_2) \tag{22}$$

$$k_1\mathbf{n}_1\cdot\nabla T_1=-k_2\mathbf{n}_1\cdot\nabla T_2 \tag{23}$$

$$\mathbf{n}_1\wedge(\mathbf{u}_1-\mathbf{u}_2)=0 \tag{24}$$

$$T_1=T_2 \tag{25}$$

where $\mathbf{n}_j$ and $\mathbf{t}_j$ are the unit outward pointing normal and tangent vectors, respectively, on interface $j$, $\mathscr{H}_j$ is the mean Gaussian curvature at interface $j$,

$$Ca_{0j}=\frac{\mu_j U}{\sigma_{0j}}$$

is the Capillary number at interface $j$, $k$ is the thermal conductivity,

$$\hat{\sigma}=\frac{\sigma_{02}}{\sigma_{01}}\quad\text{and}\quad\hat{\gamma}=\frac{\gamma_2}{\gamma_1}.$$

The surface tension coefficient $\sigma_1$ and its variation with temperature at the liquid–liquid interface was calculated, as in refs. [14, 15], using the Antonow rule [16] which states that "the surface tension between two liquids is equal to the difference between the $\sigma$ values for the respective air–liquid systems". While the validity of this approximation is questionable, at the time of this work no experimental results were available to the authors.

## 4. NUMERICAL PROCEDURE

The simulations were performed with the FIDAP code [17] based on a Galerkin finite element (GFE) technique; see also refs. [6, 17] for more details. The approach to a moving boundary involves an adaptive spatial mesh in which the nodes located on the free boundary remain on the free boundary; these nodes move along specified lines (spines). An additional degree of freedom is associated with the nodes on the free boundary which directly determines their location in space and all other interior nodes which are moved along the same lines to maintain mesh grading. Then the simultaneous calculation of the position of these nodal locations and the field variables is performed via an iterative technique. The solution procedure consists first of a successive substitution scheme (or Picard iteration), because of its large radius of convergence, and secondly, the utilization of the Newton–Raphson algorithm because of its faster convergence rate.

The computations are carried out with non-uniform (concentrated near the boundaries and interfaces) meshes of quadrilateral elements with a $C^0$ bi-quadratic approximation for the velocity and the temperature fields and a $C^{-1}$ linear approximation for the pressure.

## 5. RESULTS AND DISCUSSION

The study described herein analyzes a double layer system filled mainly with fluorinert FC75 ($Pr_1=23.38$) for the lower layer and water ($Pr_2=7.32$) for the upper layer, since they are the ones used in the physical experiments [4, 5]. This paper reports on the evolution of the flow structure when the temperature contrast between the two side walls is increased up to $\Delta T=1.1$ K, enhancing both the buoyancy and the thermocapillary forces in 1-$\boldsymbol{g}_0$ and $10^{-5}\,\boldsymbol{g}_0$ environments ($\boldsymbol{g}_0$ is the terrestrial gravitational acceleration), hereafter called 1- and $\mu$-$\boldsymbol{g}$. The space flight experiment is expected to be performed in a gravitational environment between $10^{-4}\,\boldsymbol{g}_0$ and $10^{-6}\,\boldsymbol{g}_0$. The sensitivity of the flow structure to some of the physical properties is described.

### 5.1. *Effect of the temperature gradient in a* 1-**g** *environment*

The convective heat transfer rate was studied at constant dynamic Bond numbers $Bd_1=1366$ and $Bd_2=24$, corresponding to the fluorinert FC75–water system's properties [4, 5]. Thus, the Grashof and the Marangoni numbers vary simultaneously, but at a constant ratio $Bd_j$ ($Bd_j=Gr_jPr_j/Ma_j$). Several flow configurations were obtained when increasing the Grashof numbers $Gr_1$ from 265 to $3\times10^6$ and $Gr_2$ from 24 to $2.7\times10^5$ (the Marangoni numbers ranged from 4.5 up to $5.1\times10^4$ for $Ma_1$ and from 7.3 up to $8.3\times10^4$ for $Ma_2$).

Numerous meshes have been used to perform the computations, using the mesh refinement studies done in the one layer configuration [6] for guidance. The results reported herein were obtained on six different meshes:

(1) a $51\times33$ mesh (in the $y$- and $x$-directions, respectively) for $Ma_1\leqslant170$ and $Ma_2\leqslant277$ in 1- and $\mu$-$\boldsymbol{g}$;

(2) a $51\times45$ mesh for $170<Ma_1\leqslant1.7\times10^3$ and $277<Ma_2\leqslant2.77\times10^3$ in 1-$\boldsymbol{g}$;

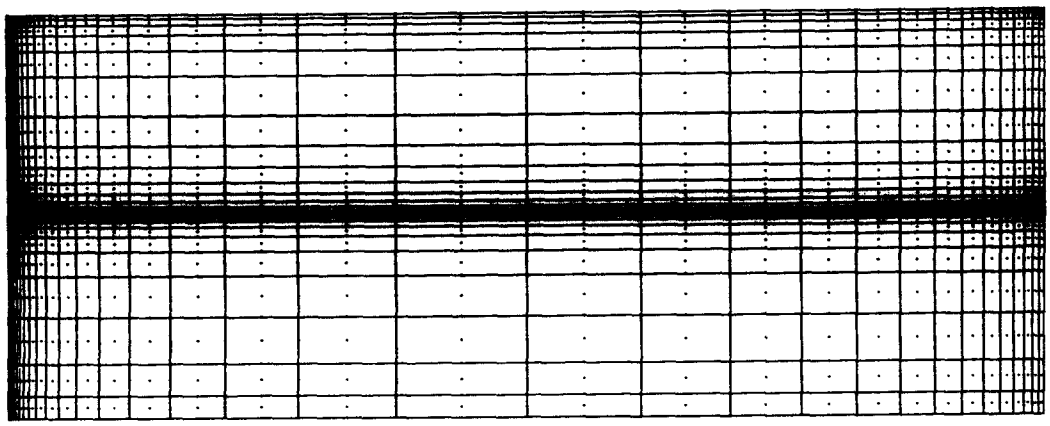

Fig. 2. Non-uniform mesh of nine node quadrilateral elements; $51 \times 73$ nodes.

(3) a $51 \times 53$ mesh for $170 < Ma_1 \leqslant 1.7 \times 10^3$ and $277 < Ma_2 \leqslant 2.77 \times 10^3$ in $\mu$-$g$;

(4) a $51 \times 73$ mesh (Fig. 2) for $1.7 \times 10^3 < Ma_1 < 1.7 \times 10^4$ and $2.7 \times 10^3 < Ma_2 < 2.8 \times 10^4$ in 1- and $\mu$-$g$;

(5) a $59 \times 73$ mesh for $Ma_1 \geqslant 1.7 \times 10^4$ and $Ma_2 \geqslant 2.77 \times 10^4$ in 1- and $\mu$-$g$;

(6) a $59 \times 109$ mesh for $Ma_1 = 5.1 \times 10^4$ and $Ma_2 = 8.3 \times 10^4$ in 1- and $\mu$-$g$ environments.

The last mesh is highly refined along the active side walls and the deformable interfaces, particularly, in the cold wall region near the free surface and the liquid–liquid interface. Such a fine mesh is needed because of the high Prandtl number fluid being considered. In this case large values of Grashof and Marangoni numbers lead to large Peclet numbers and concomitantly very small boundary layers are expected, especially for the thermal field. In addition a very complicated boundary layer structure is expected in the corner regions near the deformable interfaces. The first node in the corner region inside the fluid is at $(x = 1.283 \times 10^{-4}, y = 2A - 5.309 \times 10^{-4})$, where $(x = 0, y = 2A)$ is the point where the cold wall and the free surface intersect. Kamotani and Ostrach [18] suggested a length scale for the corner region of order $Ma^{-1}$ for a cavity filled with 10-cs silicon oil and submitted to $Ma$ in the range $10^4$–$10^5$.

For $Gr_1 = 265$, $Gr_2 = 24$, $Ma_1 = 4.5$ and $Ma_2 = 7.3$ (corresponding to $\Delta T \approx 10^{-4}$ K) the primary features one observes [Fig. 3(a)] are two large co-rotating cells (one in each liquid) with a very thin elongated counter-rotating cell inbetween at the bottom of the upper layer. The cell in the lower layer is driven both by the buoyancy force in the bulk phase augmented by a thermocapillary force at the liquid–liquid interface (flow is from the hot wall, located on the right side, to the cold one). This driving force is coupled with the flow motion of the main upper layer cell through a shear layer in the elongated cell. It is noteworthy that the surface tension gradient is almost three times larger at the free surface than at the liquid–liquid interface and one might expect a shift in structure as the gravitational force is reduced. The streamlines show similar mass transport in each fluid layer. There are two primary reasons for the occurrence of the flow separation zone in the upper layer. The first one is that the thermocapillary forces are acting to enhance the motion of the cell in the lower layer, and to retard the motion in the upper layer if no flow separation occurred and there was only a single cell in the upper layer. The second one is that the buoyancy term in the momentum equations is 22 times larger in the lower layer than in the upper one (due to larger density and volumetric coefficient of thermal expansion in the fluorinert FC75 than in water) and its buoyancy force dominates in this case; taking into account that the two fluids present a similar viscous nature ($\mu_{FC75} \approx 1.4\mu_{water}$). The thermal field is of conduction dominated type [Fig. 3(b)].

The major change is then the shift of the strongest flow velocities near the cold wall in the upper layer due to the thermocapillary forces, in the presence of contact angles equal to $\pi/2$; that occurs when $Gr_1 \geqslant 10^5$, $Gr_2 \geqslant 9.1 \times 10^3$, $Ma_1 \geqslant 1.7 \times 10^3$ and $Ma \geqslant 2.77 \times 10^3$. This typical effect for a high Prandtl number fluid has been explained in detail for the single layer model [6]; see also [10, 19–22].

Increasing the thermal gradient such that $Gr_1 = 10^6$, $Gr_2 = 9.1 \times 10^4$, $Ma_1 = 1.7 \times 10^4$ and $Ma_2 = 2.77 \times 10^4$ (corresponding to $\Delta T = 0.36$ K) leads to a flow in the upper layer, except in the separation zone, which is similar to the one obtained in the one liquid layer configuration for high Grashof and Marangoni numbers [6]. A small cell [Fig. 4(a)] is generated below the free surface near the hot wall due to surface tension forces. Close to the cold wall the streamlines are 'sucked' into the corner, reflecting a sharp surface velocity peak. This peak corresponds to the highest velocities in the entire cavity and is due to the strong thermal gradient created in the corner. These two effects are also clearly seen on the surface velocity profile [Fig. 4(d)]. It is also noteworthy that the thickness of the separation zone is decreasing when

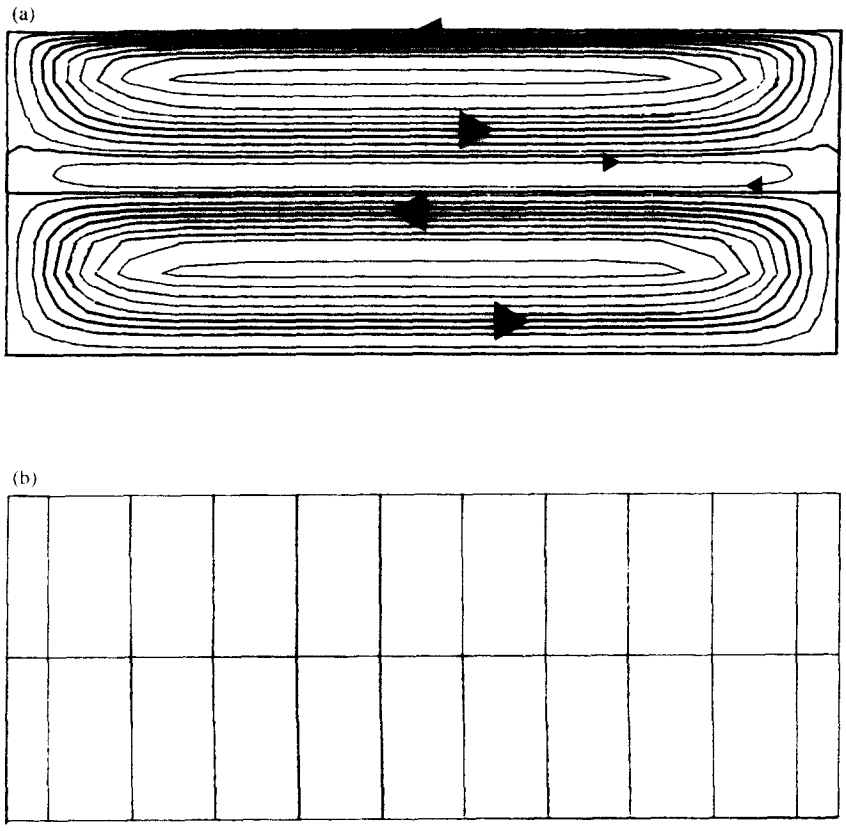


Fig. 3. The temperature gradient, streamlines (a) and isotherms (b) for $Gr_1 = 265$, $Gr_2 = 24$, $Ma_1 = 4.5$, $Ma_2 = 7.3$, $Ca_{01} = 1.28 \times 10^{-7}$, $Ca_{02} = 7.2 \times 10^{-8}$ and $Fr = 5.52 \times 10^{-11}$. $\psi_{Max} = 4.321 \times 10^{-3}$; $\psi_{min} = -4.95 \times 10^{-4}$.

increasing the thermal gradient. The horizontal velocity profile along the liquid–liquid interface [Fig. 4(c)] reflects the strong velocities which occur near the heated walls in the separation zone, an insignificant effect at smaller temperature gradients, viz, smaller Grashof and Marangoni numbers. In the lower layer one can observe a regular flow structure reflecting a horizontally stratified thermal structure [Fig. 4(a, b)]; approximately 65% of the total temperature gradient $\Delta T$ occurs near the hot wall in the bottom of the domain. Contrarily to the one liquid layer model [6], the highest velocities present in the lower liquid layer are not located very close to the cold wall like in the upper layer, but within the upward flow along the hot wall. Thus, a reduction of the thermocapillary forces near the cold wall is predicted with this two liquid layer configuration. The isotherms [Fig. 4(b)] show stronger horizontal thermal gradients along the heated walls in the lower layer ($Pr_1 = 23.38$) than in the upper one ($Pr_2 = 7.32$). This two co-rotating cell structure including a secondary cell in the upper layer has also been predicted by Ramachandran [14] for a water–hexadecane system of aspect ratio $A = 0.5$ for each layer, and by Peltier and Biringen [23] for a FC75–water system of aspect ratio $A = 1/3.81$. Similar behavior can also be noticed on the isotherms. Myrum *et al.* [15] also obtained the same type of main flow structure for a water–hexadecane configuration in a complex geometry. Azuma *et al.* [24] obtained, experimentally and numerically, this type of flow structure (two main co-rotating cells and a shear layer inbetween in the upper layer) for a fluorinert FC70–silicone oil KF96 system in a cavity of aspect ratio $A = 0.25$ for each layer, and with a stronger thermal gradient applied ($\Delta T = 10$ K). The separation zone appears to be much thinner in the experimental visualizations of Koster *et al.* [4, 5], a discrepancy which could be due to a lack of precise data for the interfacial tension of the system, or to the fact that the fluorinert–water interface is not perfectly 'clean' (as assumed in the numerical model). However this flow structure, including two co-rotating cells and the small cell created near the hot wall, is in agreement with the experiments performed for higher $\Delta T$ or when replacing water by other liquids.

When a stronger temperature gradient is imposed, the thermocapillary forces on the free surface cause the occurrence of two secondary internal cells in the upper layer with the stronger one close to the hot wall. On Fig. 5(a, b) the flow is represented when $Gr_1 = 3 \times 10^6$, $Gr_2 = 2.7 \times 10^5$, $Ma_1 = 5.1 \times 10^4$ and $Ma_2 = 8.3 \times 10^4$, corresponding to $\Delta T = 1.1$ K. (A streamline has been added on Fig. 5(a), without maintaining the difference constant between two successive

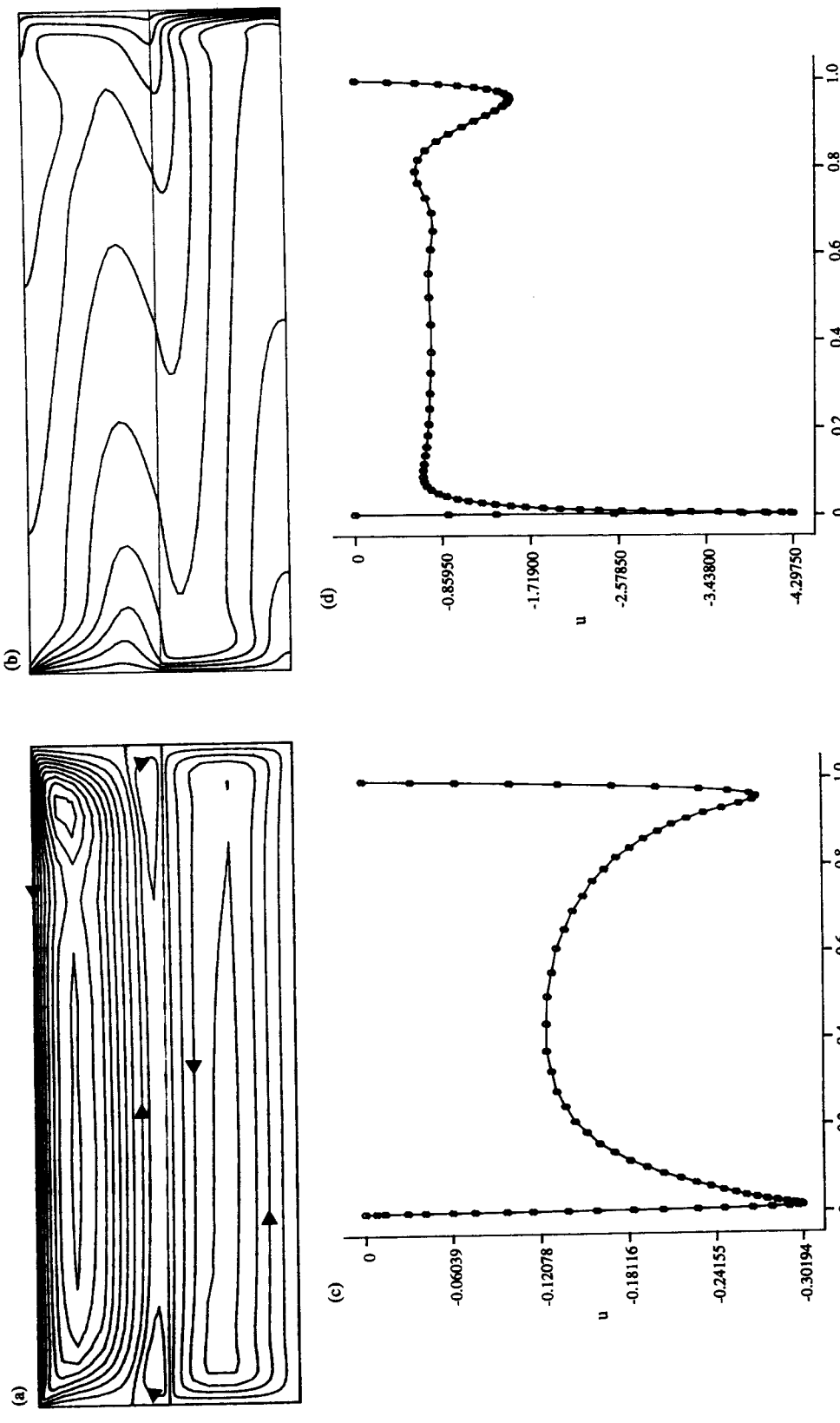


Fig. 4. Results for $Gr_1 = 10^6$, $Gr_2 = 9.1 \times 10^4$, $Ma_1 = 1.7 \times 10^4$, $Ma_2 = 2.77 \times 10^4$, $Ca_{01} = 3.1 \times 10^{-5}$, $Ca_{02} = 1.75 \times 10^{-5}$ and $Fr = 3.24 \times 10^{-6}$: streamlines (a), isotherms (b), and horizontal velocity profiles along the liquid–liquid interface (c) and the free surface (d). $\psi_{Max} = 2.38 \times 10^{-2}$; $\psi_{min} = -2.49 \times 10^{-3}$.

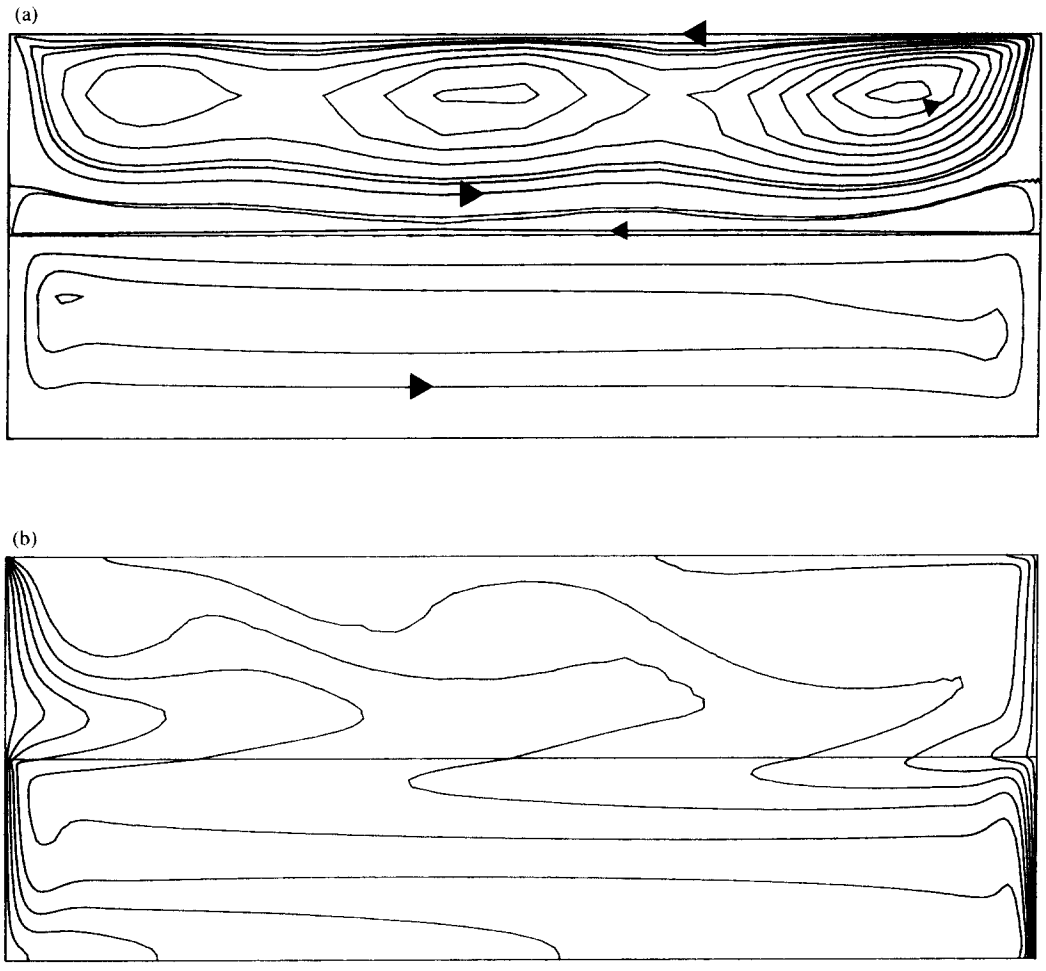


Fig. 5. The temperature gradient, streamlines (a) and isotherms (b) for $Gr_1 = 3 \times 10^6$, $Gr_2 = 2.7 \times 10^5$, $Ma_1 = 5.1 \times 10^4$, $Ma_2 = 8.3 \times 10^4$, $Ca_{01} = 6.46 \times 10^{-5}$, $Ca_{02} = 3.65 \times 10^{-5}$, and $Fr = 1.4 \times 10^{-5}$. $\psi_{Max} = 3.653 \times 10^{-2}$; $\psi_{min} = -2.3 \times 10^{-3}$.

ones in order to emphasize the flow in the lower layer.) The thickness and therefore, the motion of the separation zone is significantly affected by this three cell flow structure. The appearance of three cells is very likely due to the 'effective' aspect ratio which is decreased due to the separation zone. This flow structure has a noticeable influence on the isotherms as well as the thermal gradients close to the active walls [Fig. 5(b)]. However the primary flow in the whole cavity is still a two co-rotating cell structure. For these Grashof and Marangoni numbers the magnitude of deformation of both moving interfaces is insignificant, less than 1/2000 of the fluid depth of each layer.

A noticeable effect of the aspect ratio of the cavity on the flow structure and concomitant heat transfer has been predicted for a single layer of water submitted to a thermal contrast between the two side walls of $\Delta T = 2.5$ K under a 1-$g$ environment, that is $Gr = 6.4 \times 10^5$, $Ma = 1.5 \times 10^5$, and $Pr = 7.32$ (see ref. [25]). Two aspect ratios ($A = H/L$) were considered: a shallow cavity ($A_s = 1/5.1$), and a deeper one ($A_d = 1.525/5.1 \equiv 1/3.81$); the length $L$ was the same ($L = 5.1$ cm) for both cavities, so only the height was changed. The main feature of the flow was a cell which filled three fourths of the cavity at aspect ratio $A_d$ and half at $A_s$, while a much weaker motion was seen close to the cold wall. The isotherms reflected a broad isothermal zone (more than half of the global volume) below the free surface for the deeper cavity $A_d$. Villers and Platten [22] described also an influence of the aspect ratio in a single layer heated from one side, in the absence of gravity. (In their numerical model the free surface was considered flat and non-deformable.) When decreasing the aspect ratio $A$, a variation of the number of co-rotating internal cells is observed: a unicellular flow exists for $A = \frac{1}{2}$, a second cell occurs for $A = \frac{1}{3}$ or $A = \frac{1}{4}$, and a third cell develops for $A = \frac{1}{6}$(viz. $L = 6H$). This last structure is similar to the one obtained in our double layer system, where the 'effective' aspect ratio is very close to $A = \frac{1}{6}$. Some computations performed by Peltier and Biringen [23] utilizing a deep cavity (of aspect ratio $A_d = 1/3.81$ for each layer) for the fluorinert FC75–water system show a similar effect occurring in the water layer (upper

Table 1. Maximum of the velocity vector magnitude of the fluorinert FC75 times the surface tension gradient to the two third for the one and two layer models

| $Gr_1$ | $U_{max} \times (\partial\sigma/\partial T)^{2/3}$\|one | $U_{max} \times (\partial\sigma_1/\partial T)^{2/3}$\|two |
|---|---|---|
| $10^4$ | $6.92 \times 10^{-2}$ | $2.937 \times 10^{-2}$ |
| $10^5$ | $1.129 \times 10^{-1}$ | $4.116 \times 10^{-2}$ |
| $10^6$ | $2.414 \times 10^{-1}$ | $4.166 \times 10^{-2}$ |
| $3 \times 10^6$ | $3.163 \times 10^{-1}$ | $5.044 \times 10^{-2}$ |

one) compared to our shallower cavity $A_s$. (In their numerical model the interfaces were considered flat and non-deformable.) For a cavity of aspect ratio $A_s$ we obtained a three internal, co-rotating cell structure in the upper layer for a $\Delta T > 1$ K at 1-$g$, whereas the secondary and the third co-rotating internal cells were not observed by Peltier and Biringen [23] at the larger aspect ratio $A_d$ system, even for $\Delta T = 3$ K.

A comparison of the maximum magnitude of the velocity vector for the fluorinert FC75 between the one layer configuration and the two layer system is given in Table 1 for different temperature gradients. The variable reported is

$$\bar{U} = Uh\left(\frac{\partial\sigma_1}{\partial T}\right)^{2/3}$$

$U$ being the dimensionless value. One can notice that the motion is noticeably reduced in the lower layer when a second liquid layer is superposed above. This is to be expected when considering a multilayered system. For the one liquid layer model the velocity maximum is located on the free surface of these Grashof and Marangoni numbers, reflecting a strong surface tension effect. For the two layer model this maximum is located below the interface for $Gr_1 = 10^4$ and inside the upward mass transport along the hot wall for higher Grashof numbers, showing a buoyancy driven dominated flow for $10^5 \leqslant Gr_1 \leqslant 10^6$. When $Gr \geqslant 2 \times 10^6$ the thermocapillary forces cause the velocity to be faster at the liquid–liquid interface near the cold wall, predicting a strong thermocapillary driven effect.

### 5.2. *Effect of the temperature gradient in a $\mu$-g environment*

A micro-gravity environment was studied by considering a gravitational force of $g \approx 10^{-5} g_0$. In that case the dynamic Bond numbers $Bd_1 = 1.4 \times 10^{-2}$ and $Bd_2 = 2.5 \times 10^{-4}$ become very low. As one might expect, very different flows have been predicted in the lower layer in comparison with the 1-$g$ results.

For $Ma_1 = 4.5$, and $Ma_2 = 7.3$ ($Gr_1 = 2.7 \times 10^{-3}$, $Gr_2 = 2.5 \times 10^{-4}$, corresponding to $\Delta T \approx 10^{-4}$ K) one can see [Fig. 6(a)] a unicellular flow motion in the upper layer driven by thermocapillary forces on the free surface which are directed from the hot wall to the cold wall. The flow in the lower layer is also unicellular and counter-rotating, but very weak compared to the upper layer, suggesting that this lower cell is primarily driven by the motion in the upper layer (at 1-$g$ similar mass transports were obtained in both layers). Interfacial tension driven flows are visible in the neighborhood of the liquid–liquid interface and on the interface close to both heated walls, and create small counter-rotating rolls in these regions [Fig. 6(a)]. The maximum of the streamfunction in the lower layer is about nine times smaller (in absolute values) than in the upper one and at 1-$g$ they were approximately equal. The isotherms show a conduction dominated type of regime [Fig. 6(b)]. Thus, one can conclude that $\mu$-$g$ environment leads to a completely modified flow structure in the lower layer for the present case of a small temperature gradient.

Increasing the Marangoni numbers one observes the growth of both cells generated close to the heated walls due to thermocapillary forces acting at the liquid–liquid interface, and in particular, the right side cell (hot side) is more noticeably affected. However, a regular cell persists in the center generated by the motion of the upper layer. In this layer the surface tension effect generates the strongest velocities close to the cold wall for $Ma_2 = 2.77 \times 10^3$ ($Ma_1 = 1.7 \times 10^3$), as seen previously. Figure 7(a–d) shows the flow patterns for $Ma_1 = 1.7 \times 10^4$, $Ma_2 = 2.77 \times 10^4$, $Gr_1 = 10.2$ and $Gr_2 = 0.93$. [As in Fig. 5(a) an 'extra streamline' has been added in Fig. 7(a).] The upper layer motion is similar to the one obtained for the same Marangoni numbers under 1-g conditions, except in the vicinity of the liquid–liquid interface where the thin separated flow region does not uniformly influence the entire length. Thus, the central roll occurring in the bottom layer is still generated by the upper motion; however, this cell is weaker than the other two, i.e. the velocity and streamfunction magnitudes are smaller. The stronger one develops on the right side (hot side) and affects almost half the cavity. The ratio between the streamfunction maxima of the two liquid layers is over 13, while it was of the order of 2 in the 1-$g$ environment. The isotherms show a strongly convection dominated type of regime, reflecting the multicell flow computed [Fig. 7(b)]. Half of the temperature gradient occurs in the vicinity of the cold wall in the free surface-wall corner, causing the occurrence of the extremely large thermocapillary forces and concomitantly large velocities. Contrarily to a 1-$g$ environment, the horizontal thermal gradient is slightly higher near the hot wall in the upper layer (filled with a lower Prandtl number fluid) than in the lower layer where the thermal gradients are largely reduced.

The horizontal velocity profile is plotted along the liquid–liquid interface in Fig. 7(c) and the free surface in Fig. 7(d). Figure 7(c) reflects the effects described above, i.e. the influence of the interfacial tension driven cells. The hot cell (right side) is rotating almost twice as fast as the cold one (left side), five times the central one and extends over half the length of the cavity. The velocity maximum is about 40% higher in

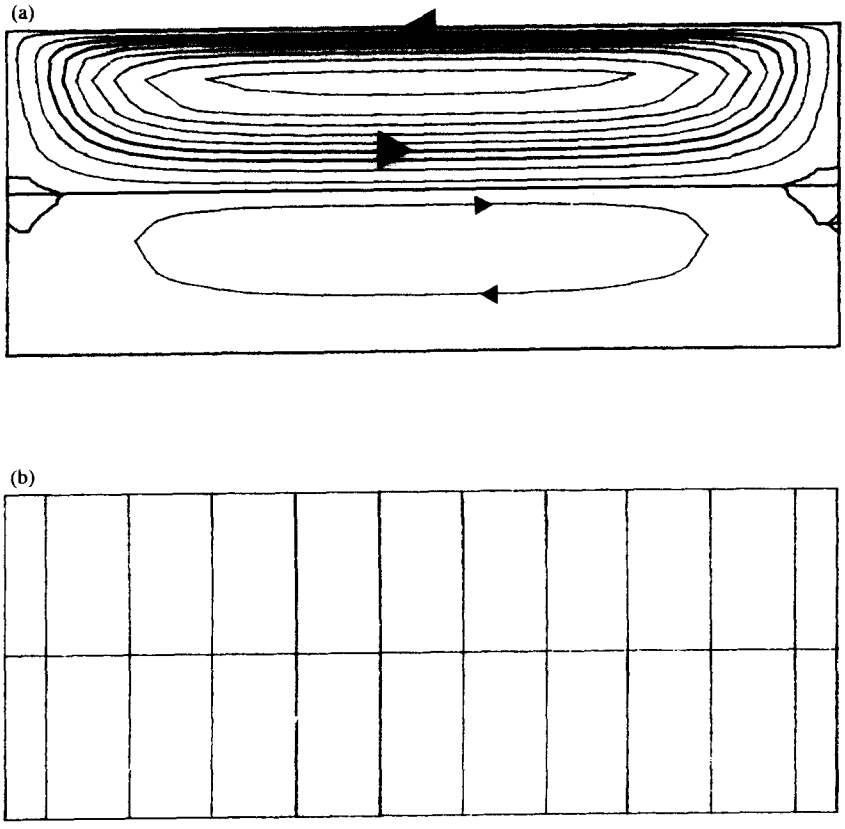


Fig. 6. Typical results for a $\mu$-$g$ environment: streamlines (a) and isotherms (b) of the flow computed at $Ma_1 = 4.5$, $Ma_2 = 7.3$, $Gr_1 = 2.7 \times 10^{-3}$, $Gr_2 = 2.5 \times 10^{-4}$, $Ca_{01} = 1.28 \times 10^{-7}$, $Ca_{02} = 7.2 \times 10^{-8}$, and $Fr = 5.42 \times 10^{-6}$, $\psi_{Max} = 5.975 \times 10^{-3}$; $\psi_{min} = -6.91 \times 10^{-4}$.

the 1-$g$ environment [Figs. 4(c), 7(c)] and this is also true for the maximum of the lower layer (Table 2). A sharp velocity peak on the free surface close to the cold wall due to the large thermal gradient [Fig. 7(b)] is seen in Fig. 7(d). The effect of the cell located near the hot wall is larger under $\mu$-$g$ conditions: the velocity maximum of the primary peak is twice the maximum of the secondary peak; this ratio was over 2.5 in 1-$g$. It is also noteworthy that the maximum of the velocity (of the primary peak which is also the maximum of the whole cavity) is only 5% smaller in $\mu$-$g$ than in 1-$g$ (Table 2).

Similar to 1-$g$ conditions secondary internal cells appear in the upper layer [Fig. 8(a, b)] for $Ma_1 = 5.1 \times 10^4$, $Ma_2 = 8.3 \times 10^4$, $Gr_1 = 30.6$ and $Gr_2 = 1.38$ ($\Delta T = 1.1$ K). [As in Figs. 5(a) and 7(a) an 'extra streamline' has been added in Fig. 8(a).] The central roll is stronger than at 1-$g$; but the major change is the presence of an extremely thin separation zone spanning the entire length of the upper layer. This proves that the thermocapillary forces created along the liquid–liquid interface become more effective than the forces generated by the flow in the upper layer, which is driven by the thermocapillary forces acting at the free surface. Thus, the lower layer has a two co-rotating cell structure in which both are driven by thermocapillarity. For the largest Marangoni numbers the magnitude of the deformation of the shape of both interfaces amounts to 1/180 of the fluid depth of each layer which is small, but larger than in 1-$g$.

The presence of very weak buoyancy forces is obvious along both active walls (lower layer), especially along the cold wall [Figs. 7(a), 8(a)], where the streamlines do not reflect the acceleration to the flow seen at 1-$g$. In terms of the isotherms [Figs. 7(b), 8(b)] this effect translates to thinner thermal boundary layers along both active walls at 1-$g$. At 1-$g$ buoyancy provides an acceleration to the flow in the vicinity of the cold wall which counteracts the adverse pressure gradient generated by the decelerating core flow, and so stabilizes the boundary layer on the lower half of the cold wall, as described by Carpenter and Homsy [19].

Table 2 contains the maxima of the velocity field in the whole cavity ($U_{max}$) and in the lower layer ($U_{l,max}$) for several Marangoni numbers. Comparison between 1-$g$ and $\mu$-$g$ environments shows that the maximum $U_{max}$ is higher at $\mu$-$g$ when $Ma_1 \leqslant 170$ and $Ma_2 \leqslant 277$. This is due to the main flow structure: two co-rotating cells and a shear layer inbetween in 1-$g$ and two counter-rotating cells in $\mu$-$g$. In the lower layer the maxima are almost three times larger in 1-g than in $\mu$-$g$ when $Ma_1 \leqslant 1.7 \times 10^3$ and $Ma_2 \leqslant 2.77 \times 10^3$, viz. when the $\mu$-$g$ motion in the whole cavity is mainly driven by the

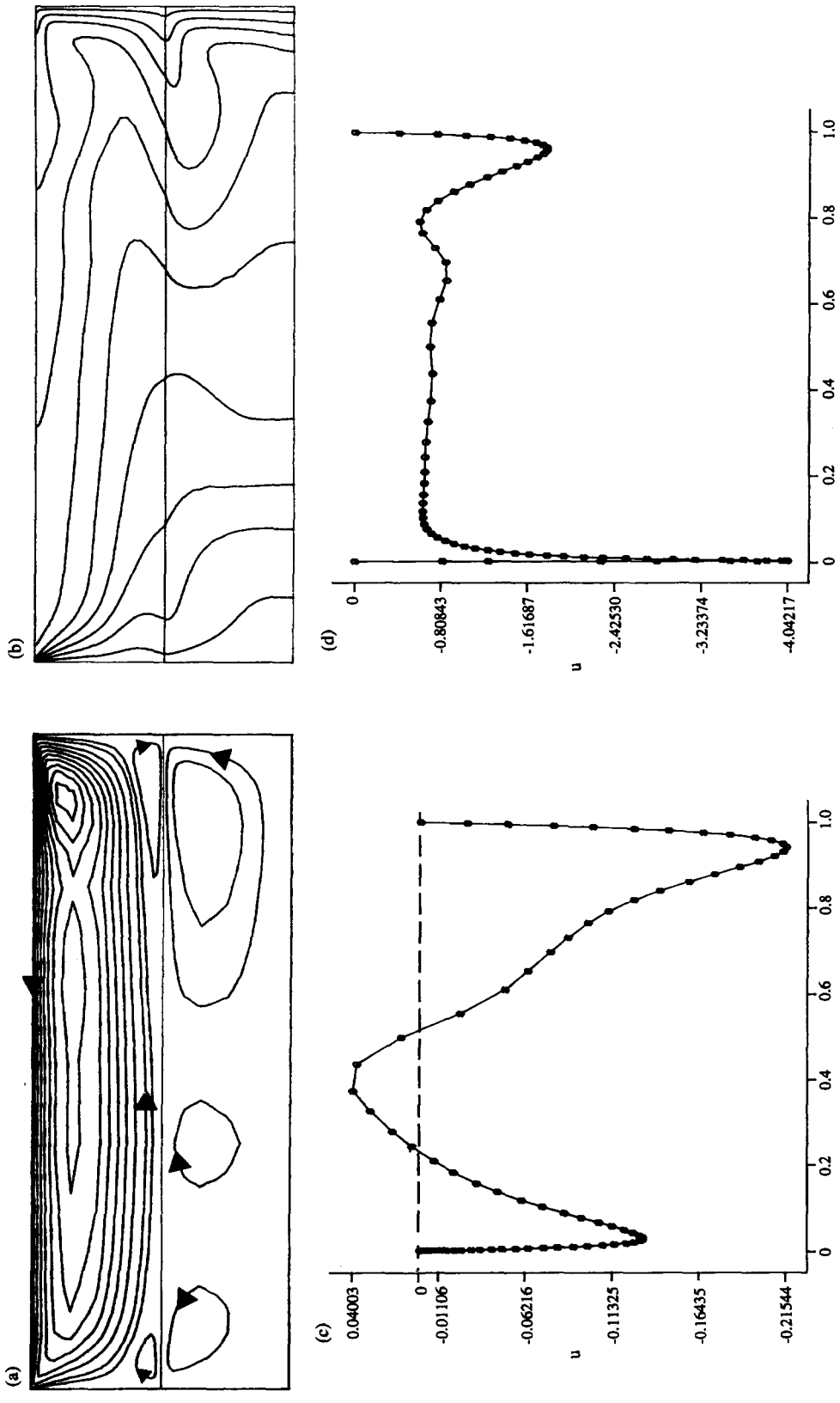


Fig. 7. Results for a $\mu$-$g$ environment for $Ma_1 = 1.7 \times 10^4$, $Ma_2 = 2.77 \times 10^4$, $Gr_1 = 10.2$, $Gr_2 = 0.93$, $Ca_{01} = 3.1 \times 10^{-5}$, $Ca_{02} = 1.75 \times 10^{-5}$, and $Fr = 3.18 \times 10^{-1}$: streamlines (a), isotherms (b), and horizontal velocity profiles along the liquid–liquid interface (c) and the free surface (d). $\psi_{\text{Max}} = 2.743 \times 10^{-2}$; $\psi_{\text{min}} = -2.06 \times 10^{-3}$.

Table 2. Maximum of the velocity and of the streamfunction of the whole cavity and of the fluorinert FC75 only ($U_{1,max}$) in 1- and $\mu$-$g$

| $Ma_1$ | $U_{max}\|1\text{-}g$ | $U_{max}\|\mu\text{-}g$ | $\psi_{max}\|1\text{-}g$ | $\psi_{max}\|\mu\text{-}g$ | $U_{1,max}\|1\text{-}g$ | $U_{1,max}\|\mu\text{-}g$ |
|---|---|---|---|---|---|---|
| 4.5 | 0.1672 | 0.1964 | 0.0043 | 0.00597 | 0.0686 | 0.024 |
| 23 | 0.2881 | 0.3371 | 0.0075 | 0.01025 | 0.1197 | 0.0414 |
| 170 | 0.6039 | 0.6475 | 0.0158 | 0.01963 | 0.2288 | 0.0793 |
| $1.7 \times 10^3$ | 1.509 | 1.338 | 0.0272 | 0.02814 | 0.3205 | 0.1142 |
| $1.7 \times 10^4$ | 4.298 | 4.042 | 0.0238 | 0.02743 | 0.3245 | 0.2154 |
| $5.1 \times 10^4$ | 5.712 | 5.479 | 0.0365 | 0.0382 | 0.3929 | 0.2608 |

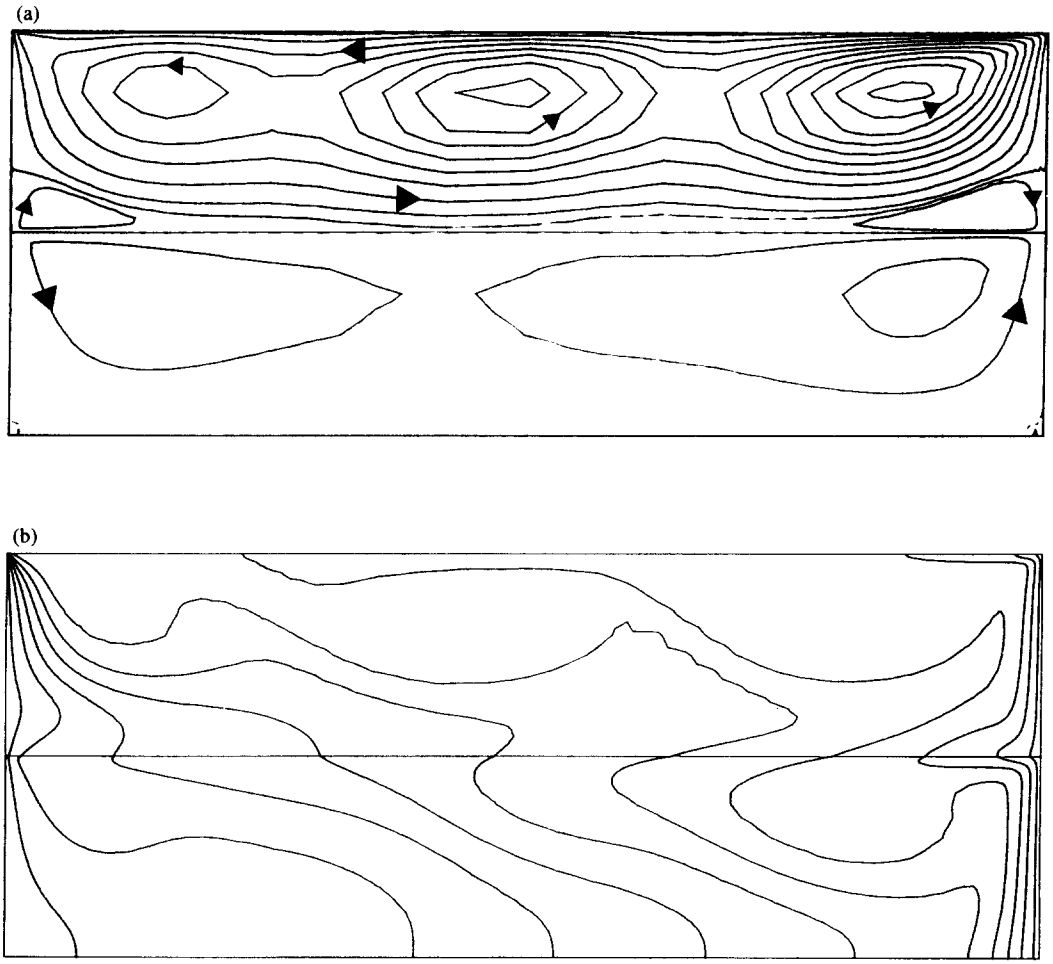


Fig. 8. The temperature gradient, streamlines (a) and isotherms (b) for a $\mu$-$g$ environment for $Ma_1 = 5.1 \times 10^4$, $Ma_2 = 8.3 \times 10^4$, $Gr_1 = 30.6$, $Gr_2 = 1.38$, $Ca_{01} = 6.46 \times 10^{-5}$, $Ca_{02} = 3.65 \times 10^{-5}$, and $Fr = 1.38$. $\psi_{Max} = 3.824 \times 10^{-2}$; $\psi_{min} = -2.54 \times 10^{-3}$.

upper layer. When the flow in the lower layer is driven predominantly by interfacial tension in $\mu$-$g$ ($Ma_1 \geqslant 1.7 \times 10^4$ and $Ma_2 \geqslant 2.77 \times 10^4$), the maxima $U_{1,max}$ are only 50% smaller than in 1-$g$. This reduction of intensity is expected when considering a multilayered system. Whereas the maximum velocity in the whole cavity $U_{max}$, located on the free surface, is only 4% smaller in $\mu$-$g$ than in 1-$g$ for $Ma_1 = 5.1 \times 10^4$ and $Ma_2 = 8.3 \times 10^4$.

Finally one can conclude that under $\mu$-g conditions the flow is weaker in the lower layer compared to 1-$g$, but almost similar (structure and intensity) in the upper layer for this fluorinert FC75–water system. These $\mu$-$g$ results are in agreement with the simulations of Crespo *et al.* [26, 27], where it has been shown that for $Ma_1 = 1/2\ Ma_2$ and in the absence of gravity the lower layer motion is very weak; when $Ma_1 = 2\ Ma_2$ the lower layer flow is stronger than the upper layer one.

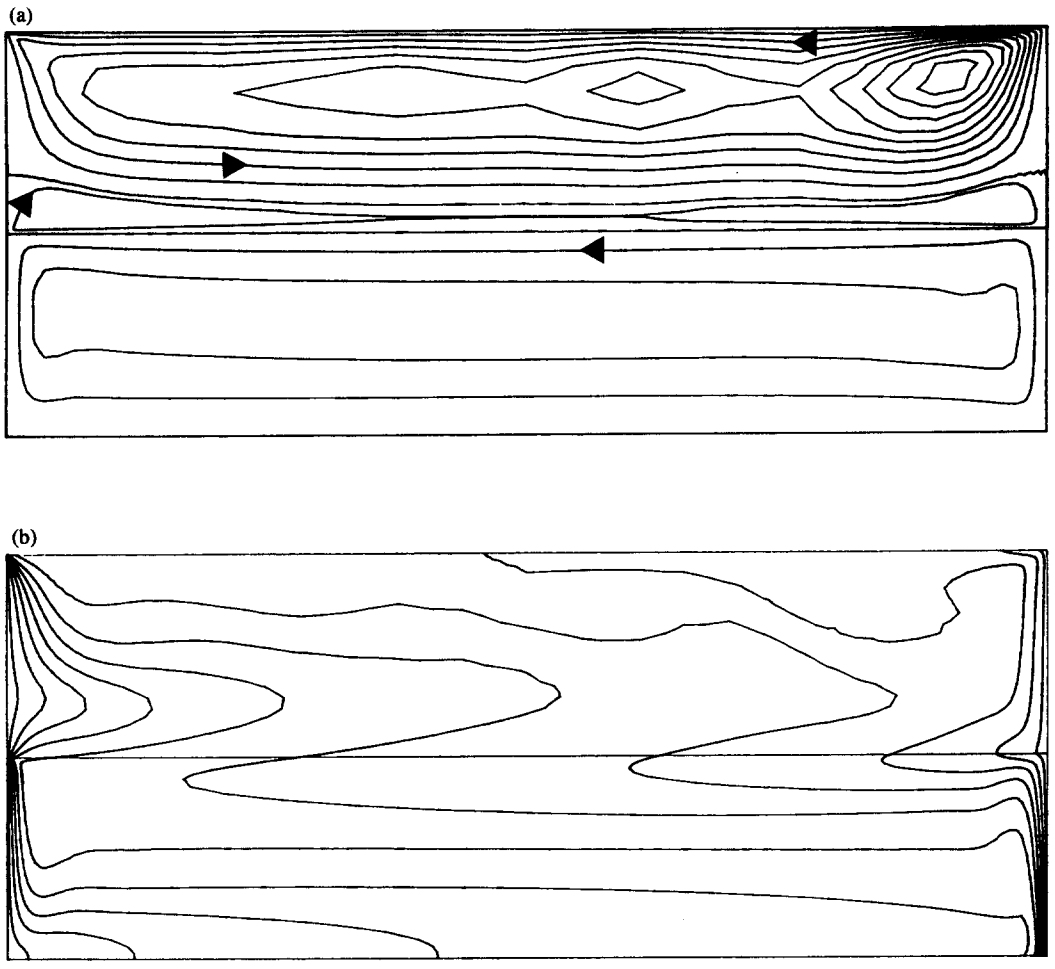


Fig. 9. Results when $\rho_2 = \rho_{water}/2$; streamlines (a) and isotherms (b) for $Gr_1 = 3 \times 10^6$, $Gr_2 = 6.8 \times 10^4$, $Ma_1 = 5.1 \times 10^4$, $Ma_2 = 8.3 \times 10^4$, $Pr_1 = 23.38$, $Pr_2 = 14.64$, $Ca_{01} = 6.46 \times 10^{-5}$, $Ca_{02} = 3.65 \times 10^{-5}$, and $Fr = 1.4 \times 10^{-5}$. $\psi_{Max} = 2.73 \times 10^{-2}$; $\psi_{min} = -2.1 \times 10^{-3}$.

5.3. *Effect of physical properties of the upper layer at* 1-**g**

The role of some physical properties of the upper layer (originally representative of water) on the flow structure was investigated for the largest temperature gradient considered $\Delta T = 1.1$ K. The $73 \times 59$ mesh was used. Here we report on the influence of the density, the viscosity and the thermal diffusivity of the upper layer, and of surface tension gradients acting at both interfaces. The main effect observed was a change in the flow structure in the top layer, in particular when varying the viscosity.

When decreasing the density, i.e. considering a fluid less dense than water, but otherwise with the same physical properties, the Prandtl number is increased and the Grashof number is decreased. Figure 9(a, b) displays the flow patterns when the density is reduced by half ($\rho_2 = \rho_{water}/2$, $Pr_2 = 14.64$, $Gr_2 = 6.8 \times 10^4$). In the top layer one observes the disappearance of the third co-rotating cell (left side) and a strong weakening of the second one. The main internal cell (near the hot wall) is reduced in size and intensity: it spreads over less than $L/4$, whereas for water it spreads over more than $L/3$, and its average angular velocity is a few % smaller. While the magnitude of the maximum velocity, located on the free surface close to the cold wall, is a few % larger (see Table 3). The separation zone is slightly thicker, and possesses a more uniform thickness because of the disappearance of the internal co-rotating cells. In the fluorinert FC75 (bottom layer) the horizontal velocities are enhanced. The maximum velocity of this lower layer is 21% larger than when $\rho_2 = \rho_{water}$, and its location on the liquid–liquid interface moves closer to the cold wall. In the upper layer the increase of the maximum velocity is less than 4% (Table 3). This effect is due to the strengthening of the thermal gradient near the cold wall visible along both interfaces [Fig. 9(b)]; such a behavior is not noticeable near the hot wall.

Modeling a less viscous flow, i.e. a smaller viscosity fluid, translates into a decrease in the Prandtl and Capillary numbers, and an increase in the Grashof and Marangoni numbers. In that case a much different flow structure is obtained. Decreasing the viscosity of

Table 3. Maximum of the velocity field in the lower layer (fluorinert-FC75) $U_{1,max}$ and in the upper layer $U_{2,max}$

| | | $\Delta T = 0.36$ K | | $\Delta T = 1.1$ K | |
|---|---|---|---|---|---|
| | | $U_{1,max}$ (cm s$^{-1}$) | $U_{2,max}$ (cm s$^{-1}$) | $U_{1,max}$ (cm s$^{-1}$) | $U_{2,max}$ (cm s$^{-1}$) |
| Single layer FC75 | 1-$g_0$ | 0.2395 | — | 0.6527 | — |
| FC75–water | 1-$g_0$ | 0.0413 | 0.5476 | 0.1041 | 1.5138 |
| FC75–water* $\rho_2 = \rho_w/2$ | 1-$g_0$ | — | — | 0.1257 | 1.5718 |
| FC75–water* $\mu_2 = 3\mu_w/4$ | 1-$g_0$ | — | — | 0.1123 | 1.9017 |
| FC75–water* $\chi_2 = \chi_w/2$ | 1-$g_0$ | — | — | 0.1227 | 1.2907 |
| FC75–water* $\partial\sigma_1/\partial T = 0$ | 1-$g_0$ | — | — | 0.075 | 1.5292 |
| FC75-water* $\partial\sigma_2/\partial T = \frac{1}{4}(\partial\sigma_w/\partial T)$ | 1-$g_0$ | — | — | 0.1132 | 0.3994 |
| FC75-water* $\partial\sigma_1/\partial T = \partial\sigma_2/\partial T = 0$ | 1-$g_0$ | — | — | 0.0741 | 0.0298 |
| FC75–water | $10^{-5}$-$g_0$ | 0.0274 | 0.515 | 0.0691 | 1.452 |

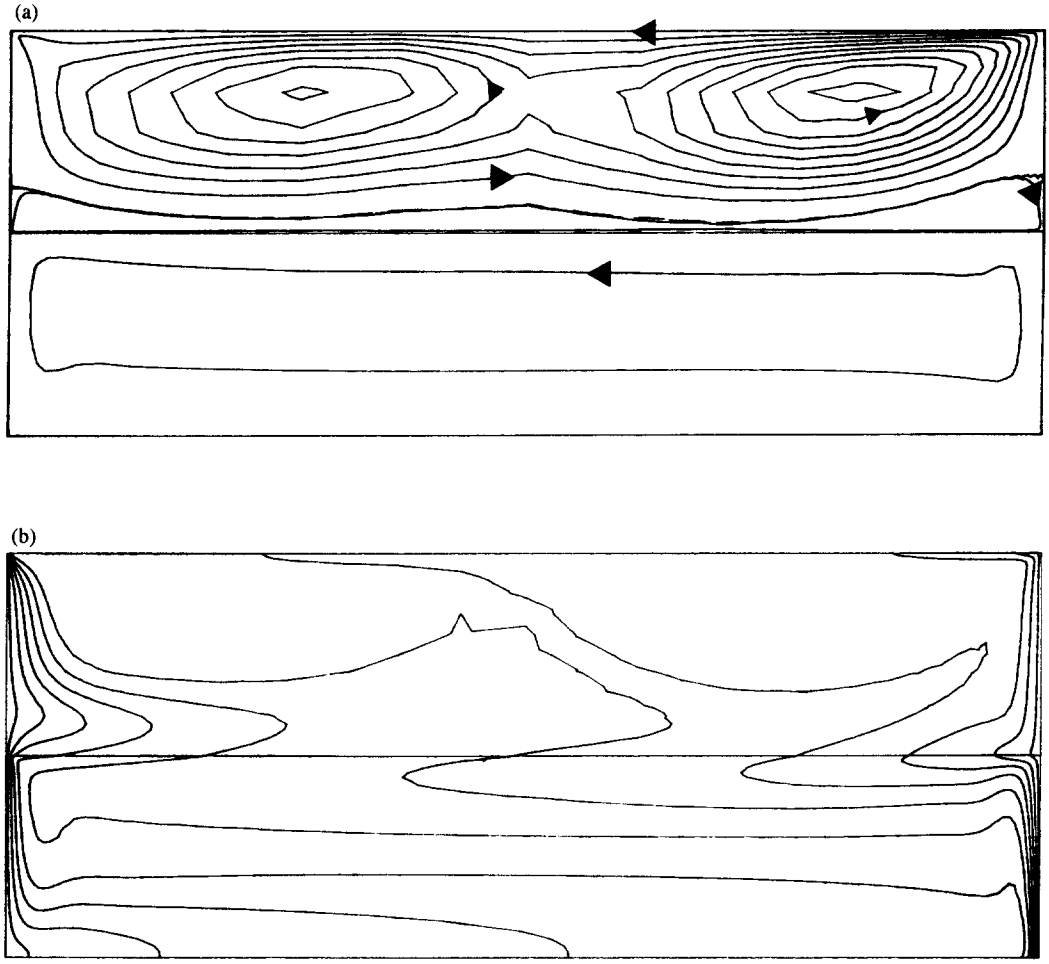


Fig. 10. Results when $\mu_2 = 3/4\mu_{water}$; streamlines (a) and isotherms (b) for $Gr_1 = 3 \times 10^6$, $Gr_2 = 4.9 \times 10^5$, $Ma_1 = 5.1 \times 10^4$, $Ma_2 = 1.1 \times 10^5$, $Pr_1 = 23.38$, $Pr_2 = 5.49$, $Ca_{01} = 6.46 \times 10^{-5}$, $Ca_{02} = 2.74 \times 10^{-5}$, and $Fr = 1.4 \times 10^{-5}$. $\psi_{Max} = 4.62 \times 10^{-2}$; $\psi_{min} = -2.63 \times 10^{-3}$.

the upper layer by one fourth ($\mu_2 = 3/4\mu_{water}$, $Pr_2 = 5.49$, $Gr_2 = 4.9 \times 10^5$, $Ma_2 = 1.1 \times 10^5$, $Ca_{02} = 2.74 \times 10^{-5}$), leads to a top layer flow structure consisting of two co-rotating cells [Fig. 10(a, b)]; both of them extend about half of the cavity. However, the cell near the hot wall is rotating twice as fast as the other one. In fact the magnitude of the velocity in the entire cavity is larger. In the upper layer the maximum velocity (located close to the cold wall on the free surface), the speed of the cell generated near the hot

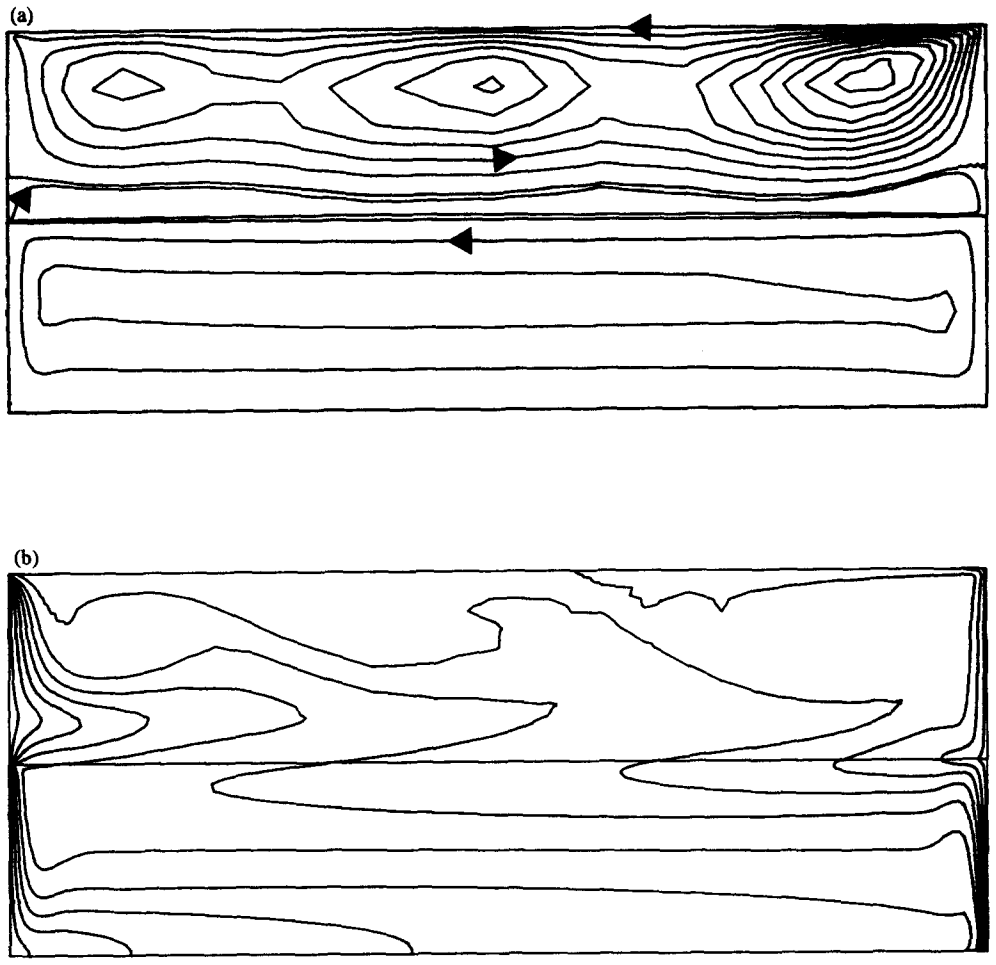


Fig. 11. Reduced thermal diffusivity in the upper layer: $\chi_2 = \chi_{water}/2$. Streamlines (a) and isotherms (b) for $Gr_1 = 3 \times 10^6$, $Ma_1 = 5.1 \times 10^4$, $Pr_1 = 23.38$, $Ca_{01} = 6.46 \times 10^{-5}$, $Gr_2 = 2.7 \times 10^5$, $Ma_2 = 1.66 \times 10^5$, $Pr_2 = 14.64$, $Ca_{02} = 3.65 \times 10^{-5}$, and $Fr = 1.4 \times 10^{-5}$. $\psi_{Max} = 2.95 \times 10^{-2}$; $\psi_{min} = -2.03 \times 10^{-3}$.

wall (measured on the free surface), and the maximum of the streamfunction (center of the right cell) are 27% larger than for the fluorinert–water system (Table 3). The lower layer (fluorinert) is affected by an increase of 8% for the maximum velocity (located on the liquid–liquid interface near the cold wall), and also for the local extremum located near the hot wall on the interface. The shape of the separation zone reflects this two cell structure, and it is similar in thickness as for the case $\mu_2 = \mu_{water}$. The major noticeable change in the isotherms [Fig. 10(b)] occurs in the central region of the upper layer where the effect of the two cell flow structure is obvious.

Decreasing the thermal diffusivity of the upper layer by a factor of two ($\chi_2 = \chi_{water}/2$), leads to a doubling of the Marangoni and Prandtl numbers. Fig. 11(a, b) displays the streamline and isotherm patterns for $Ma_2 = 1.66 \times 10^5$ and $Pr_2 = 14.64$. No major effect is observed on the flow structure; only the magnitude of different flow parameters is changed. Mainly, the transport is reduced in the upper layer causing an increase of the transport in the lower layer, as the flow intensity in the separation zone which retards the flow in the lower layer is reduced. A secondary effect is a slightly thicker separation zone, i.e. the shear layer between the two co-rotating flows in the upper and lower layers. Due to the increase in the Prandtl number, thinner thermal boundary layers are observed, causing a slight increase in the temperature gradients near the active walls: the largest increase amounts to 5% at the free surface close to the cold wall. The reduced transport causes a drop of 14% at the free surface (see Table 3) in the maximum velocity and 5% in the secondary peak near the hot wall. Thus, the maximum velocity at the liquid–liquid interface is increased by 18% (see Table 3) and moves towards the cold wall and concomitantly the thermal gradient is increased. Along the hot wall a weaker thermal gradient is observed in the lower layer, causing a 7% decrease in the secondary maximum velocity present at the liquid–liquid interface.

As expected, a more significant effect is observed when reducing the surface tension gradient at the free surface, that is reducing the thermocapillary effect. Figure 12(a, b) shows the flow when $\partial\sigma_2/\partial T$ is decreased by a factor of four leading to

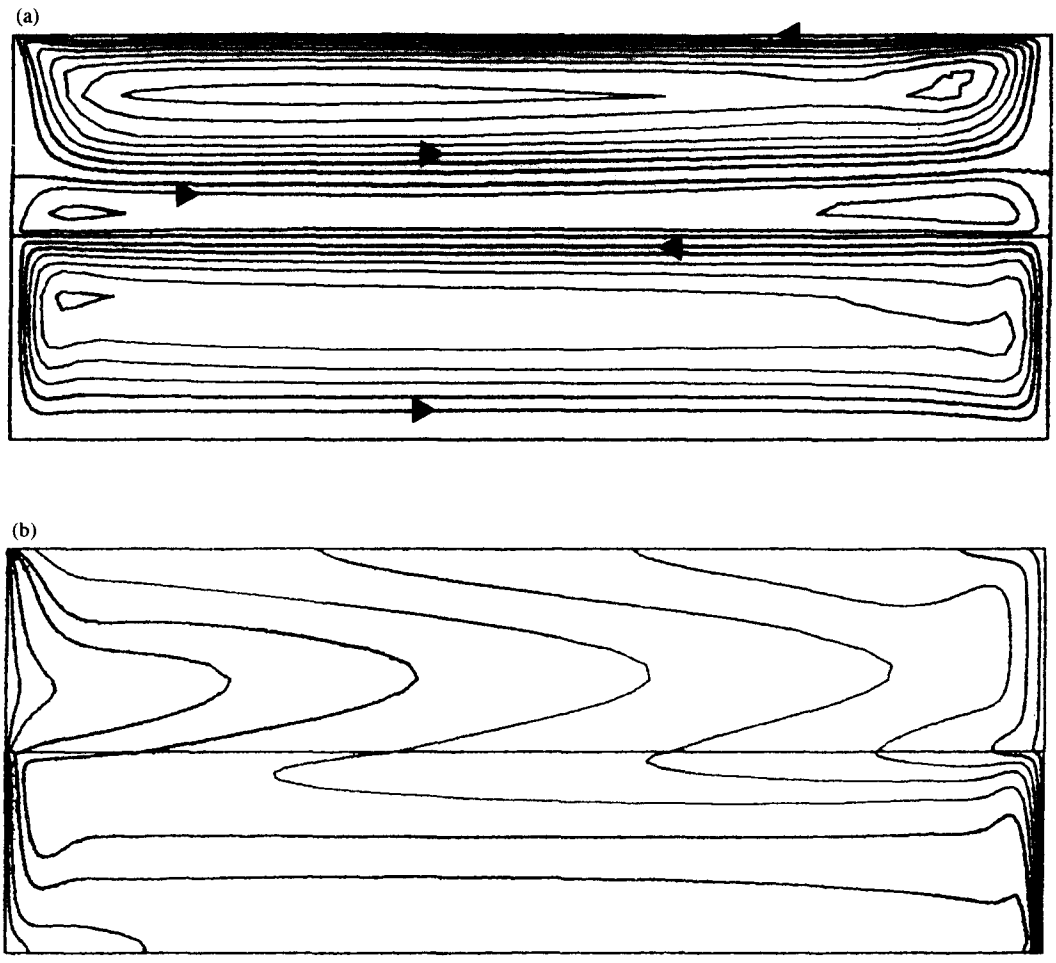


Fig. 12. Reduced surface tension gradient at the free surface:

$$\frac{\partial \sigma_2}{\partial T} = \frac{1}{4}\frac{\partial \sigma_{\text{water air}}}{\partial T}.$$

Streamlines (a) and isotherms (b) for $Gr_1 = 3 \times 10^6$, $Ma_1 = 5.1 \times 10^4$, $Pr_1 = 23.38$, $Ca_{01} = 6.46 \times 10^{-5}$, $Gr_2 = 2.7 \times 10^5$, $Ma_2 = 2.1 \times 10^4$, $Pr_2 = 7.32$, $Ca_{02} = 3.65 \times 10^{-5}$, and $Fr = 1.4 \times 10^{-5}$. $\psi_{\text{Max}} = 9.06 \times 10^{-3}$; $\psi_{\text{min}} = -2.6 \times 10^{-3}$.

$Ma_2 = 2.1 \times 10^4$. The transport in the upper layer is dramatically reduced, so that it is not much larger than in the lower layer. The ratio between the maximum velocities in both layers drops to 3.5, as compared to over 14 for the original fluorinert–water system. The weaker flow generated in the upper layer causes the occurrence of a thick separation zone at the bottom of this layer. This 'shear layer' has an almost uniform thickness and fills more than one fourth of the upper layer. With the reduction of the thermocapillary forces, one observes an elongated cell and a small internal co-rotating cell near the hot wall, as observed previously for a smaller temperature gradient. The maximum velocity peak (near the cold wall) is decreased by a factor of 3.8, as is the secondary peak located near the hot wall on the free surface and the streamfunction maximum and minimum (the latter is located inside the separation zone). In the lower layer the streamfunction maximum is similar [not seen on the Fig. 12(a) because of the drop in magnitude in the upper layer]. However the maximum velocity (near the cold wall on the free surface) is increased by almost 9%, together with a slight increase in the thermal gradient (Table 3). Near the hot wall, the thermal gradient is slightly decreased and the local maximum velocity is reduced by 2%.

As the surface tension gradient at the liquid–liquid interface is determined with the Antonow's rule because of the lack of experimental data, a configuration with a constant interfacial tension was studied to try to access the sensitivity of the results to this approximation as well as the assumption of a 'clean' interface. That means $Ma_1 = 0$, otherwise the same parameters are imposed to the flow [Fig. 13(a–d)]. The major difference in flow structure is the strong reduction of the separation zone. Without thermocapillary forces acting at the intermediate interface, a strong weakening of the temperature gradient and

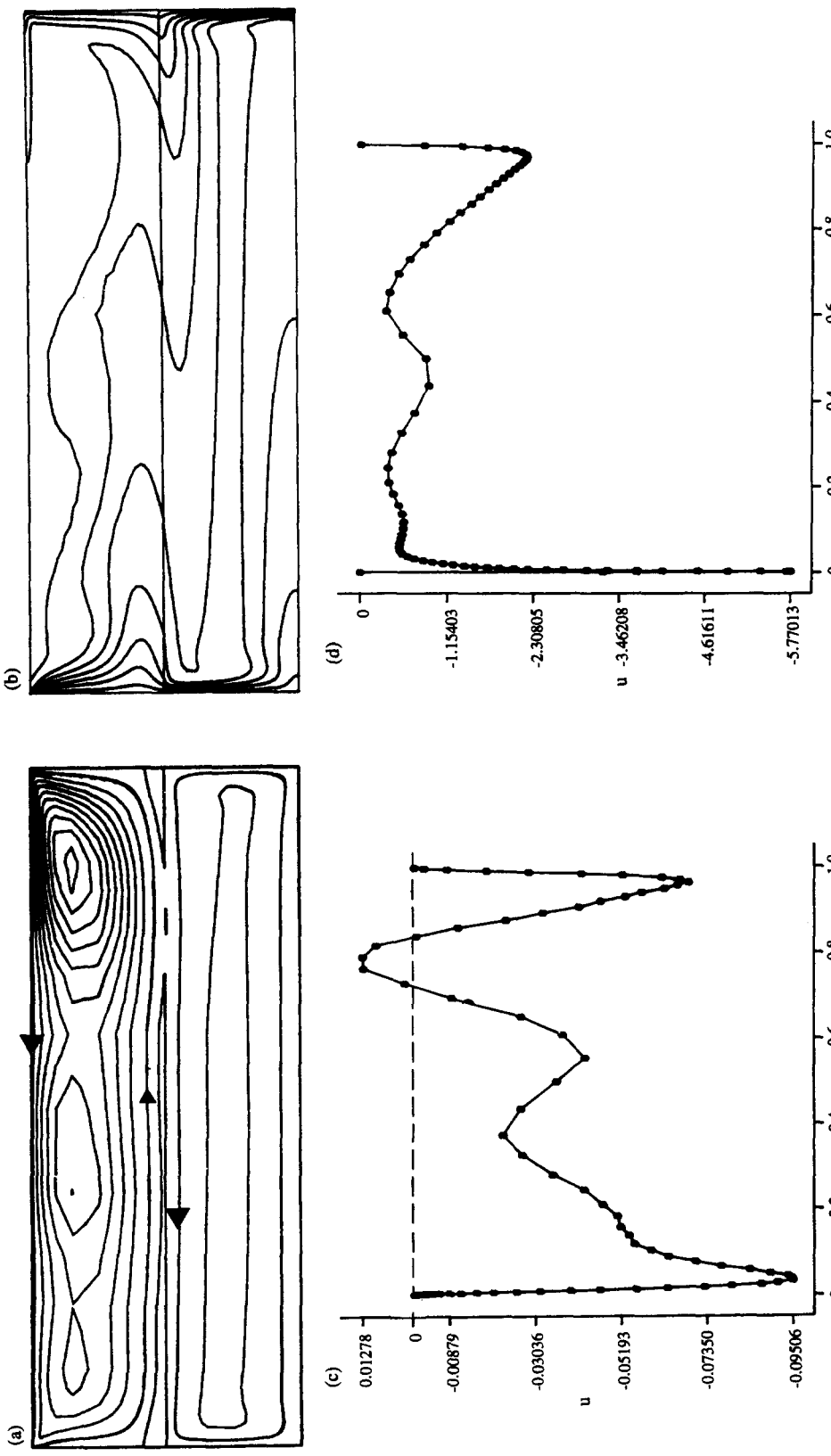


Fig. 13. Results without thermocapillary effects at the liquid–liquid interface for $Gr_1 = 3 \times 10^6$, $Ma_1 = 0$, $Pr_1 = 23.38$, $Ca_{01} = 6.46 \times 10^{-5}$, $Gr_2 = 2.7 \times 10^5$, $Ma_2 = 8.3 \times 10^4$, $Pr_2 = 7.32$, $Ca_{02} = 3.65 \times 10^{-5}$, and $Fr = 1.4 \times 10^{-5}$. Streamlines (a), isotherms (b), and horizontal velocity profiles along the liquid–liquid interface (c) and the free surface (d). $\psi_{Max} = 3.96 \times 10^{-2}$; $\psi_{min} = -5.03 \times 10^{-4}$.

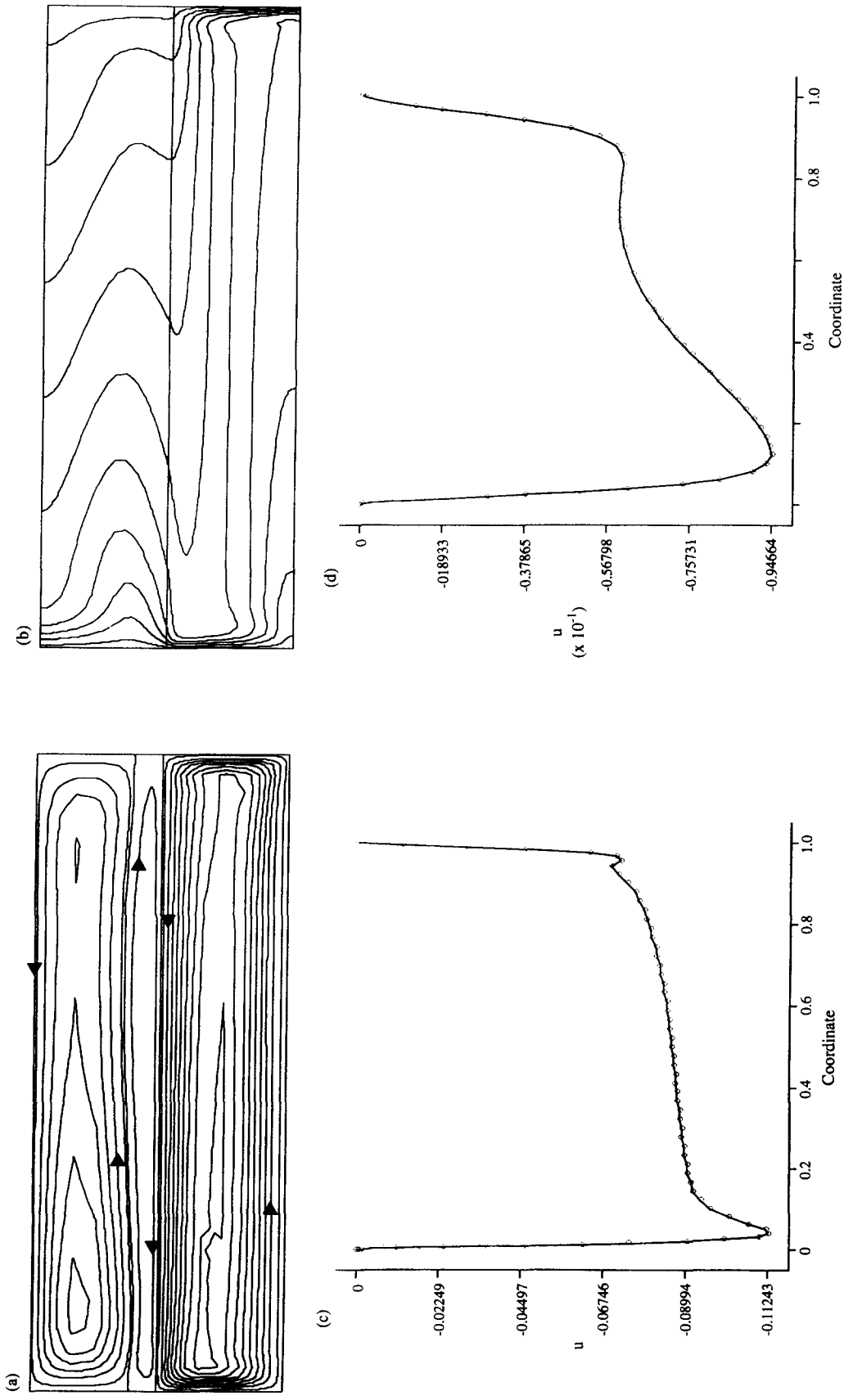


Fig. 14. Purely natural convection case for $Gr_1 = 3 \times 10^6$, $Ma_1 = 0$, $Pr_1 = 23.38$, $Ca_{01} = 6.46 \times 10^{-5}$, $Gr_2 = 2.7 \times 10^5$, $Ma_2 = 0$, $Pr_2 = 7.32$, $Ca_{02} = 3.65 \times 10^{-5}$, and $Fr = 1.4 \times 10^{-5}$. Streamlines (a), isotherms (b), and horizontal velocity profiles along the liquid–liquid interface (c) and the free surface (d). $\psi_{Max} = 6.75 \times 10^{-3}$; $\psi_{min} = -9.3 \times 10^{-4}$.

thus, the magnitude of the velocity is seen near the cold wall. The tangential velocity profile at the liquid–liquid interface [Fig. 13(c)] exhibited very low velocities. The maxima (near both heated walls) are reduced by a factor of four. The maximum velocity in the lower layer is located in the ascending flow near the hot wall. In the upper layer a slight increase of the thermal gradient is seen near the cold wall, accompanied by a maximum velocity increase of 1% (see Table 3). Otherwise the flow is similar. As the separation zone generated by shear in the upper layer is apparently not observed in the physical experiments [4, 5], one can conclude that possible reasons might be that the surface tension gradient calculated via Antonow's rule at the liquid–liquid interface is overestimated and/or the interface is 'dirty'.

In order to evaluate the relevance of the thermocapillary forces acting at both interfaces, a purely natural convection case ($Ma_1 = Ma_2 = 0$) was investigated. Figure 14(a–d) displays the flow patterns for a $71 \times 65$ mesh. In comparing this simulation to the equivalent with thermocapillarity included, it is seen that the major effect of not including the thermocapillary force is the development of a stronger mass transport in the lower layer than in the upper one, which leads to the development of a 'thick' shear layer in between (and constitutes almost one fourth of the volume of the upper layer). The isotherms result in smaller thermal gradients in the upper layer, and much thicker boundary layers (thermal and viscous) which are particularly noticeable along the fluid–fluid interfaces. This purely buoyancy driven case leads to a 29% reduction (see Table 3) in the maximum velocity in the lower layer (also the maximum velocity in the entire system). In the upper layer the maximum velocity is generated by viscosity along the liquid–liquid interface and amounts to 2% of the one created by thermocapillarity at the free surface (which was in that case the maximum velocity in the whole system). This numerical simulation shows that thermocapillarity has to be included in a model for the accurate prediction of heat and mass transport in such a multilayered system (large Prandtl numbers fluids), even in a 1-g environment.

## 6. CONCLUSIONS

This numerical study investigated the flow and concomitant thermal transport in an open cavity containing one [6] or two immiscible, shallow layers of high Prandtl number liquids. It is shown that thermocapillary forces can significantly influence the bulk flow for a high Prandtl number fluid, even in the presence of a significant gravitational force and thus need to be modeled. The system at 1-$g$ exhibits a two co-rotating cell structure in agreement with the observations of Koster *et al.* [4, 5]. A comparison at 1-$g$ between a single liquid layer configuration (fluorinert FC75) and a two liquid layer system (fluorinert FC75–water) shows a significantly reduced flow in the lower layer when encapsulated (also true for a fluorinert FC75–ethylene glycol combination, see Part II). The sensitivity of the flow structure to the viscosity, the density and the thermal diffusivity of the encapsulant layer is reflected primarily by the intensity of the flow in the lower layer at 1-$g$; for example, even a different flow structure is obtained in the upper layer when decreasing the viscosity. Under $\mu$-$g$ conditions, the strength of the flow in the lower layer is significantly reduced and a multicellular flow structure appears, despite the fact that nearly the same maximum velocity occurs at the free surface. The effect of some thermal conditions applied to the present cavity is discussed in Part II, as well as the influence of another encapsulant liquid which is more viscous by an order of magnitude than water. Additional transient computations to determine the flow stability of the multilayered system including a deformable interface would provide additional insight into the mechanism of the instability.

*Acknowledgements*—We wish to acknowledge Professor J. Koster and A. Prakash for collaboration during the course of this work, and P. Bontoux and E. Crespo del Arco for interesting discussion. We wish to thank also the support of the European Space Agency (through a Fellowship to J.-P.F.), of the Centre National d'Etudes Spatial (through a Fellowship to J.-P.F.), of the Center for Low-Gravity Fluid Mechanics and Transport Phenomena, of the National Science Foundation under grant no. CTS-9120673 (R.L.S.), of the Conseil Régional de Provence-Alpes-Côte-d'Azur, and of the GDR-MFN (Groupement de Recherche de Mécanique des Fluides Numérique G0138-CNRS).

## REFERENCES

1. S. Ostrach and A. Pradhan, Surface-tension induced convection at reduced gravity, *AIAA J.* **16**, 419–424 (1978).
2. Y. Kamotani, S. Ostrach and M. Vargas, Oscillatory thermocapillary convection in a simulated floating-zone configuration, *J. Crystal Growth* **66**, 83–90 (1984).
3. J.-P. Fontaine, A. Randriamampianina and P. Bontoux, Numerical simulation of flow structures and instabilities occurring in a liquid-encapsulated Czochralski process, *Phys. Fluids* **3**, 2310–2331 (1991).
4. J. N. Koster, A. Prakash, D. Fujita and T. Doi, Bénard and Marangoni convection in immiscible liquid layers, *ASME 28th National Heat Transfer Conf.*, 9–12 August, San Diego, CA (1992).
5. J. N. Koster, A. Prakash, T. A. Campbell and A. Pline, Analysis of convection in immiscible liquid layers with novel particle tracking velocimetry, *ASME* 1992 *WAM*, 8–13 November, Anaheim, CA (1992).
6. J.-P. Fontaine, J. Koster and R. L. Sani, Thermocapillary effects in a shallow cavity filled with high Prandtl number fluids, *Annales Chimie-Sci. Matér.* **17**, 377–388 (1992) (France).
7. J.-P. Fontaine and R. L. Sani, Thermocapillary effects in a multilayered fluid system, *AIAA paper* 92-0689, *AIAA 30th Aerospace Sciences Meeting*, Reno, Nevada (1992).
8. J.-P. Fontaine and R. L. Sani, High Prandtl number fluids in a multilayered system under 1-g or $\mu$-g environment, *Proceedings of the VIIIth European Symp. on Materials and Fluid Sciences in Microgravity*, ESA SP-333, pp. 197–202 (1992).
9. J. R. Keller and T. L. Bergman, Thermocapillary cavity

convection in wetting and nonwetting liquids, *Numer. Heat Transfer*, Part A **18,** 33–49 (1990).
10. Y. Kamotani, Thermocapillary flow in a square cavity with curved liquid free surface, AIAA paper 88-3726, 1792–1797 (1988).
11. C. Cuvelier and J. M. Driessen, Thermocapillary free boundaries in crystal growth, Delft University of Technology Report 85–17 (1985).
12. S. Ostrach, Motion induced by capillarity, *Phys. Chem. Hydrodyn.* **2,** 571–589 (1977).
13. S. Ostrach, Convection due to surface-tension gradients, *Space Res.* **19,** 563–570 (1979).
14. N. Ramachandran, Thermal buoyancy and Marangoni convection in a two fluid layered system—a numerical study, AIAA paper 90-0254, Vol. 30, 812–821, A90-19756 (1990).
15. T. A. Myrum, E. M. Sparrow and A. T. Prata, Numerical solutions for natural convection in a complex enclosed space containing either air–liquid or liquid–liquid layers, *Numer. Heat Transfer* **10,** 19–43 (1986).
16. J. J. Bikerman, *Physical Surfaces*. Academic Press, New York (1970).
17. M. Engelman, *FIDAP Users Manual*. Fluid Dynamics International, Evanston, Illinois (1990).
18. Y. Kamotani and S. Ostrach, Design of a thermocapillary flow experiment in reduced gravity, *J. Thermophys.* **1,** 83–89 (1987).
19. B. M. Carpenter and G. M. Homsy, Combined buoyant-thermocapillary flow in a cavity, *J. Fluid Mech.* **207,** 121–132 (1989).
20. A. Zebib, G. M. Homsy and E. Meiburg, High Marangoni number convection in a square cavity, *Phys. Fluids* **28,** 3467–3476 (1985).
21. J. C. Chen, J. C. Sheu and S. S. Jwu, Numerical computation of thermocapillary convection in a rectangular cavity, *Numer. Heat Transfer*, Part A **17,** 287–308 (1990).
22. D. Villers and J. K. Platten, Coupled buoyancy and Marangoni convection in acetone: experiments and comparison with numerical simulations, *J. Fluid Mech.* **234,** 487–510 (1992).
23. L. J. Peltier and S. Biringen, Numerical simulation of time-dependent thermocapillary convection in layered fluid systems, *J. Thermophys. Heat Transfer (ASME)* (in press).
24. H. Azuma, S. Yoshihara, M. Ohnishi and T. Doi, Upper layer flow phenomena in two immiscible liquid layers subject to a horizontal temperature gradient, *Proceedings of the IUTAM Symp. on Microgravity Fluid Mechanics*, Bremen, Germany (Edited by H. J. Rath), pp. 205–212 (1991).
25. J. P. Fontaine, Flow and transport in a multilayered fluid system, E.S.A. report (1992).
26. E. Crespo del Arco, G. P. Extrémet and R. L. Sani, Thermocapillary convection in a two-layer fluid system with flat interface, *Adv. Space Res.* **11,** 129–132 (1991).
27. E. Crespo del Arco, G. P. Extrémet and R. L. Sani, Steady thermocapillary flows in a two-layer liquid system with flat interfaces, *J. Crystal Growth* **126,** 335–346 (1993).